Aided Inertial Navigation of Small Unmanned Aerial Vehicles Using an Ultra-Wideband Real Time Localization System

Krzysztof Cisek
krzysztof.cisek@ntnu.no

Kristoffer Gryte
kristoffer.gryte@ntnu.no

Torleiv H. Bryne
torleiv.h.bryne@ieee.org

Tor A. Johansen
tor.arne.johansen@ntnu.no

Centre for Autonomous Marine Operations and Systems (NTNU AMOS)
Department of Engineering Cybernetics
Norwegian University of Science and Technology

Abstract— This paper presents an ultra-wideband (UWB) radio aided inertial navigation system (INS), estimating position, velocity and attitude (PVA), based on a low-cost micro-electro-mechanical system (MEMS) Inertial Measurement Units (IMUs). This ensures that a drift free INS is available for local unmanned aerial vehicle (UAV) navigation independent of global navigation satellite systems (GNSS). The experimental results show that the presented integration of UWB and INS is promising for navigating independent of satellite-based positioning systems, and illustrates the possible enhancements that are possible when adding an additional vertical position measurement.

TABLE OF CONTENTS

1. INTRODUCTION

The de facto sensor used to aid inertial navigation systems (INS) in outdoor environments in high-accuracy applications has been real time kinematic (RTK) global navigation satellite system (GNSS) positioning, which provides centimeter-level accuracy within $20\,\mathrm{km}$ of the RTK base station, [1]. However, RTK is known to be prone to loss of carrier-phase integer-ambiguity fix and is also exposed to GNSS denial of service, due to interference or no line of sight to a sufficient number of satellites. In recent years another sensor applicable for INS position aiding has emerged; Ultra-wideband (UWB) radio based real time location system (RTLS). UWB refers to radios with a spectrum bandwidth of at least $500\,\mathrm{MHz}$ or 20%

of their center frequency [2]. This enables access to a redundant positioning principle independent of GNSS applicable for usage in local positioning of industrial robots [3], terminal and warehouse containers [4] together with applications in patient care and in construction sites [5].

RTLS has an unique ability to determine three dimensional (3D) position of a tag in space, in real or close to real time [6]. UWB RTLS has several properties that are beneficial for INS aiding: Its small footprint [7] makes it ideal for small UAVs. The GHz-wide frequency band makes it robust and less prone to multipath, which is advantageous for cluttered environments and low altitude flights. The short pulse of the UWB signal enables low energy consumption, as well as a high data-rate (up to $2\,\mathrm{Mbps}$). The technology also allows for a high density of devices [7], which is an advantage for the scalability of the system. In addition, the user also has full control of the positioning system, in contrast to satellite systems that are controlled by governmental entities. Additionally, satellite systems are dependent on atmospheric conditions from satellite to receiver. UWB RTLS may also be installed in GNSS denied environments, for instance under bridges or indoor environments, and could provide INS aiding in the event of GNSS denial of service. One consequence of using UWB for localization is the need to place anchors in the vicinity of the operation, since the range of the radio communication is limited, typically to several hundred meters. For cluttered environments, a more severe drawback is likely to be effects from non-line-of-sight measurements. This leads to a delay in the measurements, causing a bias, which requires special consideration [8, 9]. In general, UWB RTLS is applicable in short-range navigation, where fast response, robustness and precision is needed.

This paper is an extension of the initial work of [10], in which the design and implementation of the UWB nodes are presented in detail, along with a comparison of least-square based position estimation algorithms. Further, this paper also extends the previous work of [11], where the focus was on the integration of RTK, INS and UWB, merely with simulation studies. This paper seeks to join the previous efforts by utilizing an observer for tight integration of UWB range measurement together with inertial measurements, on data from real flight test experiments, using an unmanned aerial vehicle (UAV). Moreover, the tight integration of inertial and UWB range measurements is beneficial for multiple reasons: Since the position measurements in tight integration is expressed in the range space, which enables a more fine-grained
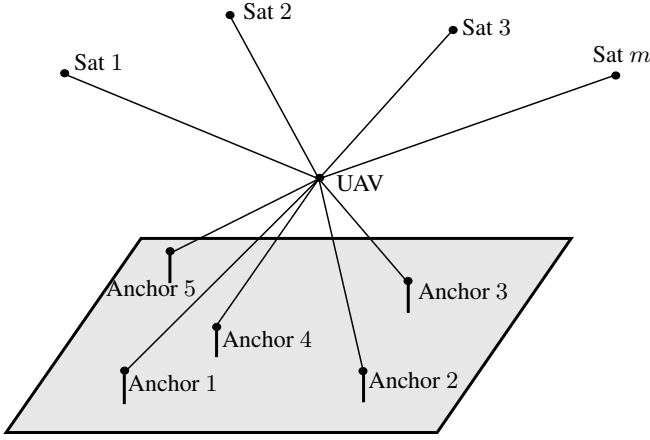
Figure 1. UWB ranging concept.

outlier detection compared to loose integration. If one of the range measurements is unreasonable, that measurement can be rejected, while the sensible measurements still can be used in the estimate. This is contrary to loose integration, with measurements in the position-space, where the entire position estimate would be rejected.

The tight integration of UWB pseudoranges and inertial measurements can also be considered a first step towards tight integration with GNSS, which will substantially improve the geometry of the ranging problem compared to an only-GNSS solution since ranges originate both above and below the navigating UAV. Furthermore, with tight integration, one cascade of estimators is avoided by eliminating the need to estimate the position before the integration with inertial sensors, as is the case in loose integration. Moreover, integration of sensors in the position-space potentially violates the basic assumption of white measurement noise, which is the foundation of many estimators such as the Kalman filter. This stems from the fact that the errors of the position output of a range-based estimator will not be Gaussian. Nevertheless, such position estimates are often used as aiding measurements in the context of loose INS integration.

A large drawback with RTK GNSS, in addition to the disadvantages related to operation in GNSS-denied areas, is the potentially time consuming process of correctly solving the integer ambiguities for the carrier-phase measurements, i.e. arriving at a *fixed* solution. This can be particularly problematic for highly dynamic platforms, and when the satellite constellation is poor. These problems are mitigated by an integrated UWB-inertial solution, which, despite the slightly less accurate estimates, makes it a viable solution e.g. for UAV landing in areas at high latitude.

Notable previous attempts at using UWB ranges in inertial navigation include [12] and [13], where in the latter, a moving quadcopter achieves a position error of only 41 mm, in an indoor lab. The focus of this work is on the use of UWB aiding in an outdoor environment. A practical problem when using UWB ranging in large scale experiments in the field, is the placement of the anchors. It is impractical to spread the anchors in the vertical plane, leading to poor geometry of the ranging problem. Thus, the accuracy of the navigation solution can be greatly improved by adding ranging information from an additional sensor that is vertically separated from the UWB anchors. Examples of such sensors are barometric pressure, altimeter laser, radar and ultrasound, which can

provide range measurements to the ground.

Main Contribution

In this paper the concept of tightly integrated UWB RTLS and INS is presented using an nonlinear observer framework with exponential stability properties and is validated experimentally. The experimental demonstration is carried out by comparing two measurement setups; one that uses UWB ranging to aid the IMU, and another that also uses the height information embedded in the RTK GPS output as a range measurement to the earth center, as a proof of concept.

Organization

The paper is organized by first presenting some preliminaries (Section 2), before moving on to a presentation of the nonlinear observer framework based for tightly coupled UWB/INS integration (Section 3). Then the experiment setup (Section 4) is presented before the results (Section 5) are presented. Finally, the results of the paper are summarized (Section 6).

2. PRELIMINARIES

Before presenting algorithms and the accompanying results, some preliminaries are stated.

Notation

The Euclidean vector norm is denoted $\| \cdot \|_2$. The $n \times n$ identity matrix is denoted $\boldsymbol{I}_n$, while a block diagonal matrix is given by $\boldsymbol{M} = \text{blockdiag}(\boldsymbol{M}_1, \boldsymbol{M}_2, \ldots, \boldsymbol{M}_n)$ for square matrices $\boldsymbol{M}_1$ to $\boldsymbol{M}_n$. Moreover, the transpose of a vector or a matrix is denoted $(\cdot)^\mathsf{T}$. Coordinate frames are denoted with $\{\cdot\}$. $\boldsymbol{S}(\cdot) \in SS(3)$ represents the skew symmetric matrix such that $\boldsymbol{S}(\boldsymbol{z}_1)\boldsymbol{z}_2 = \boldsymbol{z}_1 \times \boldsymbol{z}_2$ for two vectors $\boldsymbol{z}_1, \boldsymbol{z}_2 \in \mathbb{R}^3$. $\boldsymbol{z} = (\boldsymbol{z}_1; \boldsymbol{z}_2; \ldots; \boldsymbol{z}_n)$ denotes a vector of stacked column vectors $\boldsymbol{z}_1, \boldsymbol{z}_2, \ldots \boldsymbol{z}_n$. In addition, $\boldsymbol{z}_{bc}^a \in \mathbb{R}^3$ denotes a vector $\boldsymbol{z}$, to frame $\{c\}$, relative $\{b\}$, decomposed in $\{a\}$. Moreover, $\otimes$ denotes the Hamiltonian quaternion product. Saturation is represented by $\text{sat}_{(\cdot)}$, where the subscript indicates the saturation limit.

A geometric range is denoted with ρ, being the Euclidean vector norm of the difference of two given vectors $\boldsymbol{z}_1, \boldsymbol{z}_2$, i.e. $\rho = \|\boldsymbol{z}_1 - \boldsymbol{z}_2\|_2$. The rotation matrix, $\boldsymbol{R}_a^b \in SO(3)$, describes the rotation between two given frames $\{a\}$ and $\{b\}$. Equivalently, the rotation between $\{a\}$ and $\{b\}$ may be represented using the unit quaternion $\boldsymbol{q}_a^b = (s, \boldsymbol{r}^\mathsf{T})^\mathsf{T}$ where $s \in \mathbb{R}^1$ is the real part of the quaternion and $\boldsymbol{r} \in \mathbb{R}^3$ is the vector part. In addition, the Euler angles are given as

$$\boldsymbol{\Theta} = (\phi, \quad \theta, \quad \psi)^\mathsf{T}, \quad (1)$$

where ϕ is the roll angle, θ is the pitch angle, and ψ is the yaw angle. Latitude and longitude on Earth is represented by $\mu \in [-\pi/2, \pi/2]$ and $\lambda \in (-\pi, \pi]$, respectively.

Coordinate Frames

This paper considers four coordinate frames; The Earth Centered Inertial (ECI) frame, the Earth Centered Earth Fixed (ECEF) frame, a local Earth-fixed North East Down (NED) frame, and the BODY reference frame, denoted $\{i\}$, $\{e\}$, $\{n\}$, and $\{b\}$, respectively (see Fig. 2).
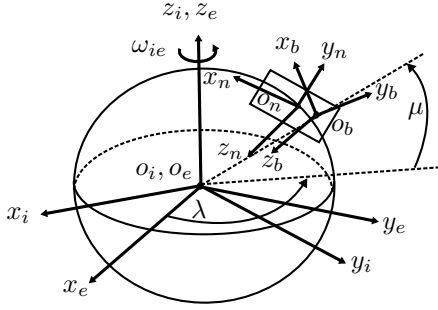
Figure 2. Definitions of the BODY, NED, ECEF and ECI reference frames.

Strapdown Equations

The NLO-based INS is derived using

$$\dot{\boldsymbol{p}}_{eb}^e = \boldsymbol{v}_{eb}^e \tag{2}$$

$$\dot{\boldsymbol{v}}_{eb}^e = -2\boldsymbol{S}(\boldsymbol{\omega}_{ie}^e)\boldsymbol{v}_{eb}^e + \boldsymbol{R}_b^e\boldsymbol{f}_{ib}^b + \boldsymbol{g}_b^e(\mu,\lambda) \tag{3}$$

$$\dot{\boldsymbol{q}}_b^e = \frac{1}{2}\boldsymbol{q}_b^e \otimes \begin{pmatrix} 0 \\ \boldsymbol{\omega}_{ib}^b \end{pmatrix} - \frac{1}{2}\boldsymbol{q}_b^e \otimes \begin{pmatrix} 0 \\ \boldsymbol{\omega}_{it}^e \end{pmatrix} \tag{4}$$

as strapdown equations, with $\boldsymbol{\omega}_{ie}^e = (0,\,0,\,1)^{\mathsf{T}}\,\omega_{ie}$, where ω_{ie} is the earth's rotation rate.

Inertial Measurement Units

A simplified measurement model of an IMU can be given as

$$\boldsymbol{f}_{\mathrm{IMU}}^b = \boldsymbol{f}_{ib}^b + \boldsymbol{b}_{\mathrm{acc}}^b + \boldsymbol{w}_{\mathrm{acc}}^b \tag{5}$$

$$\boldsymbol{\omega}_{\mathrm{IMU}}^b = \boldsymbol{\omega}_{ib}^b + \boldsymbol{b}_{\mathrm{ars}}^b + \boldsymbol{w}_{\mathrm{ars}}^b \tag{6}$$

where $\boldsymbol{f}_{ib}^b$ is the specific force, relating to the acceleration and gravity vector, $\boldsymbol{g}_b^e(\mu,\lambda)$ through

$$\begin{aligned} \boldsymbol{f}_{ib}^b &= \boldsymbol{R}_e^b\dot{\boldsymbol{v}}_{ib}^e - \boldsymbol{R}_e^b\boldsymbol{g}_b^e(\mu,\lambda) \\ &= \boldsymbol{a}_{ib}^b + \boldsymbol{S}(\boldsymbol{\omega}_{ib}^b)\boldsymbol{v}_{ib}^b - \boldsymbol{R}_e^b\boldsymbol{g}_b^e(\mu,\lambda) \end{aligned} \tag{7}$$

$\boldsymbol{\omega}_{ib}^b$ represents angular velocity, while $\boldsymbol{v}_{ib}^b$, represents the BODY-fixed linear velocity. The BODY-fixed acceleration is represented by $\boldsymbol{a}_{ib}^b$, while $\boldsymbol{S}(\boldsymbol{\omega}_{ib}^b)\boldsymbol{v}_{ib}^b$ constitutes the centripetal accelerations. The biases in the accelerometer and angular rate sensor are denoted $\boldsymbol{b}_{\mathrm{acc}}^b$ and $\boldsymbol{b}_{\mathrm{ars}}^b$, respectively, while $\boldsymbol{w}_{\mathrm{acc}}^b$ and $\boldsymbol{w}_{\mathrm{ars}}^b$ represent the corresponding Gaussian white noise terms.

Pseudorange measurements

Since the UWB range calculations are based on timing of the signal transmitted from the anchor to the tag, the UWB systems provide pseudorange measurements, and not the true geometric range.

The pseudorange measurement to the kth UWB anchor may therefore be given as

$$y_{k_{\mathrm{UWB}}} = \|\boldsymbol{p}_{eb}^e - \boldsymbol{p}_{eb,k_{\mathrm{UWB}}}^e\|_2 + \beta_{\mathrm{UWB}}, \tag{8}$$

where $\boldsymbol{p}_{eb}^e$ the vehicle's position, while $\boldsymbol{p}_{eb,k_{\mathrm{UWB}}}^e$ represent the kth anchor position For UWB systems based on measurements of the Time-of-Arrival (TOA), inter anchor/tag clock synchronization errors will effect the pseudorange calculation. This effect is included in the measurement equation

through β_{UWB} representing the clock error of the UWB tag. Moreover, β_{UWB}, is modeled as a slowly drifting parameter

$$\dot{\beta}_{\mathrm{UWB}} = 0. \tag{9}$$

3. NONLINEAR OBSERVER FOR AIDED INS

The UAV's position, velocity and attitude (PVA) is estimated using a feedback-interconnected nonlinear observer integration strategy, based on the work of [14, 15] and references therein, depicted in fig. 3. The first part being a nonlinear observer (NLO), estimating attitude and ARS biases. The second part is a translational motion observer (TMO), estimating the position, velocity and specific force in ECEF coordinates, based on inertial measurements and the attitude provided by the NLO. The estimated specific force is further provided to the NLO and used to improve the attitude estimates.

Attitude Observer

The NLO for estimating the attitude between the $\{b\}$ and the $\{e\}$ frame is given similar to [14, 15], fusing accelerometer, ARS and magnetometer measurements.

$$\Sigma_1 : \begin{cases} \dot{\hat{\boldsymbol{q}}}_b^e = \frac{1}{2}\hat{\boldsymbol{q}}_b^e \otimes \begin{pmatrix} 0 \\ \hat{\boldsymbol{\omega}}_{ib}^b \end{pmatrix} - \frac{1}{2}\begin{pmatrix} 0 \\ \boldsymbol{\omega}_{ie}^e \end{pmatrix} \otimes \hat{\boldsymbol{q}}_b^e, & (10a) \\[2mm] \hat{\boldsymbol{\omega}}_{ib}^b = \boldsymbol{\omega}_{\mathrm{IMU}}^b - \hat{\boldsymbol{b}}_{\mathrm{ars}}^b + \hat{\boldsymbol{\sigma}}_{ib}^b, & (10b) \\[2mm] \dot{\hat{\boldsymbol{b}}}_{\mathrm{ars}}^b = \mathrm{Proj}\left(\hat{\boldsymbol{b}}_{\mathrm{ars}}^b - k_I\hat{\boldsymbol{\sigma}}_{ib}^b\right), & (10c) \end{cases}$$

where $\mathrm{Proj}(\cdot)$ denotes the angular rate bias projection algorithm ensuring that $\|\hat{\boldsymbol{b}}_{\mathrm{ars}}^b\|_2 \leq M_{\hat{b}_{\mathrm{ars}}}$ where $M_{\hat{b}_{\mathrm{ars}}} > M_{b_{\mathrm{ars}}}$ [16] for some upper bound $M_{b_{\mathrm{ars}}}$ on the gyro bias, and where k_I is the gain associated with the rate gyro bias estimation.

The specific force and magnetometer measurements are utilized to correct the attitude estimate and estimate the ARS bias through the observer's nonlinear injection term, $\hat{\boldsymbol{\sigma}}_{ib}^b$, given as

$$\hat{\boldsymbol{\sigma}}_{ib}^b = k_1\underline{\boldsymbol{v}}_1^b \times \boldsymbol{R}^{\mathsf{T}}(\hat{\boldsymbol{q}}_b^e)\underline{\boldsymbol{v}}_1^e + k_2\underline{\boldsymbol{v}}_2^b \times \boldsymbol{R}^{\mathsf{T}}(\hat{\boldsymbol{q}}_b^e)\underline{\boldsymbol{v}}_2^e, \tag{11}$$

where the measurement vectors $\underline{\boldsymbol{v}}_{1,2}^b$ and reference vectors $\underline{\boldsymbol{v}}_{1,2}^e$ are calculated using

$$\underline{\boldsymbol{v}}_1^b = \underline{\boldsymbol{f}}^b, \qquad \underline{\boldsymbol{v}}_1^e = \underline{\boldsymbol{f}}^e, \tag{12}$$

$$\underline{\boldsymbol{v}}_2^b = \underline{\boldsymbol{f}}^b \times \underline{\boldsymbol{m}}^b, \quad \underline{\boldsymbol{v}}_2^e = \underline{\boldsymbol{f}}^e \times \underline{\boldsymbol{m}}^e. \tag{13}$$

Furthermore, the measurement and corresponding reference vector pairs in (12)–(13) are constructed as

$$\underline{\boldsymbol{f}}^b = \frac{\boldsymbol{f}_{\mathrm{IMU}}^b}{\|\boldsymbol{f}_{\mathrm{IMU}}^b\|_2}, \quad \underline{\boldsymbol{f}}^e = \frac{\mathrm{sat}_{M_f}(\hat{\boldsymbol{f}}_{ib}^e)}{\|\mathrm{sat}_{M_f}(\hat{\boldsymbol{f}}_{ib}^e)\|_2}, \tag{14}$$

$$\underline{\boldsymbol{m}}^b = \frac{\boldsymbol{m}_{\mathrm{mag}}^b}{\|\boldsymbol{m}_{\mathrm{mag}}^b\|}, \quad \underline{\boldsymbol{m}}^e = \frac{\boldsymbol{m}_{eb}^e}{\|\boldsymbol{m}_{eb}^e\|}. \tag{15}$$

$\boldsymbol{m}_{eb}^e$ is the known magnetic field in the ECEF frame, while $\hat{\boldsymbol{f}}_{ib}^e$ is the estimated specific force, provided by the TMO, as depicted in fig. 3 and presented next in Sec. 3. The estimated
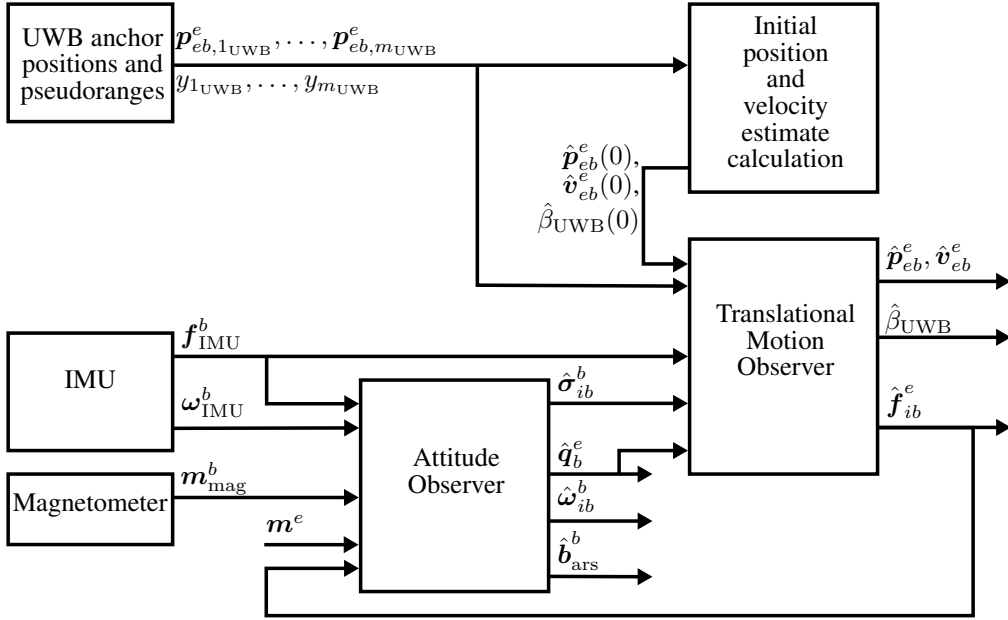
Figure 3. NLO structure overview.

specific force is saturated by M_f, an upper bound on the specific force. The normalized vector configuration in equation (14) and (15) was chosen such that the vector pairs become dimensionless and, hence, only provide direction, such that the gains $k_{1,2}$ can be considered as cut-off frequencies of the complementary filter Σ_1, [17]. Since the gains have unit rad/s, $\hat{\boldsymbol{\sigma}}_{ib}^b$ obtains the same unit as $\boldsymbol{\omega}_{\mathrm{IMU}}^b$.

Translational Motion Observer

The TMO is similar to that of [15], except that aiding measurements from UWB is added and given as follows,

$$\Sigma_2 : \begin{cases} \dot{\hat{\boldsymbol{p}}}_{eb}^e = \hat{\boldsymbol{v}}_{eb}^e + \sum_{k=1}^{m_{\mathrm{UWB}}} \boldsymbol{K}_{k,\mathrm{UWB}}^{pp} \tilde{y}_{k,\mathrm{UWB}} & (16a) \\[2mm] \dot{\hat{\boldsymbol{v}}}_{eb}^e = -2\boldsymbol{S}(\boldsymbol{\omega}_{ie}^e)\boldsymbol{v}_{eb}^e + \hat{\boldsymbol{f}}_{ib}^e + \boldsymbol{g}_b^e(\hat{\boldsymbol{p}}_{eb}^e) \\ \qquad + \sum_{k=1}^{m_{\mathrm{UWB}}} \boldsymbol{K}_{k,\mathrm{UWB}}^{vp} \tilde{y}_{k,\mathrm{UWB}} & (16b) \\[2mm] \dot{\boldsymbol{\xi}}_{ib}^e = -\boldsymbol{R}(\hat{\boldsymbol{q}}_b^e)\boldsymbol{S}(\hat{\boldsymbol{\sigma}}_{ib}^b)\boldsymbol{f}_{\mathrm{IMU}}^b \\ \qquad + \sum_{k=1}^{m_{\mathrm{UWB}}} \boldsymbol{K}_{k,\mathrm{UWB}}^{\xi p} \tilde{y}_{k,\mathrm{UWB}} & (16c) \\[2mm] \hat{\boldsymbol{f}}_{ib}^e = \boldsymbol{R}(\hat{\boldsymbol{q}}_b^e)\boldsymbol{f}_{\mathrm{IMU}}^b + \boldsymbol{\xi}_{ib}^e, & (16d) \\[2mm] \dot{\hat{\beta}}_{\mathrm{UWB}} = \sum_{k=1}^{m_{\mathrm{UWB}}} \boldsymbol{K}_{k,\mathrm{UWB}}^{\beta_{\mathrm{UWB}}p} \tilde{y}_{k,\mathrm{UWB}} & (16e) \end{cases}$$

where

$$\tilde{y}_{k,\mathrm{UWB}} = y_{k_{\mathrm{UWB}}} - \left(\hat{\rho}_{k,\mathrm{UWB}} + \hat{\beta}_{\mathrm{UWB}} \right),$$

with

$$\hat{\rho}_{k_{\mathrm{UWB}}} = \|\hat{\boldsymbol{p}}_{eb}^e - \boldsymbol{p}_{eb,k_{\mathrm{UWB}}}^e\|, \qquad (17)$$

and while $\boldsymbol{K}_{k,\mathrm{UWB}}^{\dagger p}$ is a gain associated with the kth UWB pseudorange measurements. Here, superscript $\dagger$ is a placeholder used to signify which state the gain corresponds to,

while the superscript p indicates that the gain corresponds to a position-based measurement [15]. Further, m_{UWB} denotes the number of UWB anchors, while $\boldsymbol{\xi}_{ib}^e$ is an auxiliary state used to estimate $\boldsymbol{f}_{ib}^e$. By noting the linear time-varying (LTV) structure of (16) and defining

$$\boldsymbol{x} := (\boldsymbol{p}_{eb}^e; \quad \boldsymbol{v}_{eb}^e; \quad \boldsymbol{\xi}_{ib}^e; \quad \beta_{\mathrm{UWB}}), \qquad (18)$$

the TMO can be written on LTV form as

$$\dot{\hat{\boldsymbol{x}}} = \boldsymbol{A}\hat{\boldsymbol{x}} + \boldsymbol{B}(t)\boldsymbol{u} + \boldsymbol{D}(t,\hat{\boldsymbol{x}}) + \boldsymbol{K}(t)(\boldsymbol{y} - \hat{\boldsymbol{y}}(\hat{\boldsymbol{x}})), \quad (19)$$

with the system matrices,

$$\boldsymbol{A} = \begin{pmatrix} \boldsymbol{0}_{3\times3} & \boldsymbol{I}_3 & \boldsymbol{0}_{3\times3} & \boldsymbol{0}_{3\times1} \\ \boldsymbol{0}_{3\times3} & \boldsymbol{0}_{3\times3} & \boldsymbol{I}_3 & \boldsymbol{0}_{3\times1} \\ \boldsymbol{0}_{3\times3} & \boldsymbol{0}_{3\times3} & \boldsymbol{0}_{3\times3} & \boldsymbol{0}_{3\times1} \\ \boldsymbol{0}_{1\times3} & \boldsymbol{0}_{1\times3} & \boldsymbol{0}_{1\times3} & 0 \end{pmatrix}, \qquad (20)$$

$$\boldsymbol{B}(t) = \begin{pmatrix} \boldsymbol{0}_{3\times3} & \boldsymbol{0}_{3\times3} \\ \boldsymbol{R}(\hat{\boldsymbol{q}}_b^e) & \boldsymbol{0}_{3\times3} \\ \boldsymbol{0}_{3\times3} & \boldsymbol{R}(\hat{\boldsymbol{q}}_b^e) \\ \boldsymbol{0}_{1\times3} & \boldsymbol{0}_{1\times3} \end{pmatrix}, \qquad (21)$$

$$\boldsymbol{C}(t) = \begin{pmatrix} \frac{(\hat{\boldsymbol{p}}_{eb}^e - \boldsymbol{p}_{eb,1_{\mathrm{UWB}}}^e)^\mathsf{T}}{\hat{\rho}_{1_{\mathrm{UWB}}}} & \boldsymbol{0}_{1\times3} & \boldsymbol{0}_{1\times3} & 1 \\ \frac{(\hat{\boldsymbol{p}}_{eb}^e - \boldsymbol{p}_{eb,2_{\mathrm{UWB}}}^e)^\mathsf{T}}{\hat{\rho}_{2_{\mathrm{UWB}}}} & \boldsymbol{0}_{1\times3} & \boldsymbol{0}_{1\times3} & 1 \\ \vdots & \vdots & \vdots & \vdots \\ \frac{(\hat{\boldsymbol{p}}_{eb}^e - \boldsymbol{p}_{eb,m_{\mathrm{UWB}}}^e)^\mathsf{T}}{\hat{\rho}_{m_{\mathrm{UWB}}}} & \boldsymbol{0}_{1\times3} & \boldsymbol{0}_{1\times3} & 1 \end{pmatrix}, \quad (22)$$

the measurement vector and estimated measurement vector,

$$\boldsymbol{y} = \begin{pmatrix} y_{1_{\mathrm{UWB}}} \\ y_{2_{\mathrm{UWB}}} \\ \vdots \\ y_{m_{\mathrm{UWB}}} \end{pmatrix}, \quad \hat{\boldsymbol{y}} = \begin{pmatrix} \hat{\rho}_{1_{\mathrm{UWB}}} + \hat{\beta}_{\mathrm{UWB}} \\ \hat{\rho}_{2_{\mathrm{UWB}}} + \hat{\beta}_{\mathrm{UWB}} \\ \vdots \\ \hat{\rho}_{m_{\mathrm{UWB}}} + \hat{\beta}_{\mathrm{UWB}} \end{pmatrix}, \quad (23)$$

4

with, $\hat{\rho}_{k_{\text{UWB}}}$ given in (17), the vector,

$$\boldsymbol{D}(t,\hat{\boldsymbol{x}}) = (\boldsymbol{0}_{3\times1}; \quad -2\boldsymbol{S}(\boldsymbol{\omega}_{ie}^e)\hat{\boldsymbol{v}}_{eb}^e + \boldsymbol{g}_b^e; \quad \boldsymbol{0}_{3\times1}; \quad 0).$$
(24)

The gain matrix

$$\boldsymbol{K}(t) = \begin{pmatrix} K_{1,\text{UWB}}^{pp} & K_{2,\text{UWB}}^{pp} & \cdots & K_{m_{\text{UWB}},\text{UWB}}^{pp} \\ K_{1,\text{UWB}}^{vp} & K_{2,\text{UWB}}^{vp} & \cdots & K_{m_{\text{UWB}},\text{UWB}}^{vp} \\ K_{1,\text{UWB}}^{\zeta p} & K_{2,\text{UWB}}^{\zeta p} & \cdots & K_{m_{\text{UWB}},\text{UWB}}^{\zeta p} \\ K_{1,\text{UWB}}^{\beta_{\text{UWB}}p} & K_{2,\text{UWB}}^{\beta_{\text{UWB}}p} & \cdots & K_{m_{\text{UWB}},\text{UWB}}^{\beta_{\text{UWB}}p} \end{pmatrix},$$

is updated by solving the Riccati-equation

$$\frac{1}{\vartheta}\boldsymbol{P}(t) = \boldsymbol{A}\boldsymbol{P}(t) + \boldsymbol{P}(t)\boldsymbol{A}^\mathsf{T} - \boldsymbol{P}(t)\boldsymbol{C}^\mathsf{T}(t,\boldsymbol{x})\boldsymbol{R}^{-1}(t)\boldsymbol{C}^\mathsf{T}(t,\boldsymbol{x})\boldsymbol{P}(t)$$
$$+ \boldsymbol{E}(t)\boldsymbol{Q}(t)\boldsymbol{E}^\mathsf{T}(t),$$
(25)

with

$$\boldsymbol{E}(t) = \begin{pmatrix} \boldsymbol{B}(t) & \boldsymbol{0}_{9\times1} \\ & 1 \end{pmatrix},$$
(26)

and with $\boldsymbol{R}(t)$ and $\boldsymbol{Q}(t)$ being symmetric, positive definite and possibly time-varying matrices, for a $\boldsymbol{P}(t) = \boldsymbol{P}^\mathsf{T}(t) > 0$, to obtain

$$\boldsymbol{K}(t) = \boldsymbol{P}(t)\boldsymbol{C}^\mathsf{T}(t)\boldsymbol{R}^{-1}(t).$$

Finally, the input is given as

$$\boldsymbol{u} = \left(\boldsymbol{f}_{\text{IMU}}^b; -\boldsymbol{S}(\hat{\boldsymbol{\sigma}}_{ib}^b)\boldsymbol{f}_{\text{IMU}}^b\right).$$
(27)

Moreover, the error states of the TMO can be defined as $\tilde{\boldsymbol{p}}_{eb}^e := \boldsymbol{p}_{eb}^e - \hat{\boldsymbol{p}}_{eb}^e$, $\tilde{\boldsymbol{v}}_{eb}^e := \boldsymbol{v}_{eb}^e - \hat{\boldsymbol{v}}_{eb}^e$, and $\tilde{\boldsymbol{f}}_{eb}^e := \boldsymbol{f}_{ib}^e - \hat{\boldsymbol{f}}_{ib}^e$, where the latter is obtained through a combination of (16c)–(16d), the resulting the error state is obtained,

$$\tilde{\boldsymbol{x}} := \left(\tilde{\boldsymbol{p}}_{eb}^e; \quad \tilde{\boldsymbol{v}}_{eb}^e; \quad \tilde{\boldsymbol{f}}_{ib}^e; \quad \tilde{\beta}_{\text{UWB}}\right).$$
(28)

The corresponding error dynamics of the origin of Σ_2 is then obtained as

$$\dot{\tilde{\boldsymbol{x}}} = (\boldsymbol{A} - \boldsymbol{K}(t)\boldsymbol{C}(t))\tilde{\boldsymbol{x}} + \boldsymbol{\rho}_1(t,\tilde{\boldsymbol{x}}) + \boldsymbol{\rho}_2(t,\boldsymbol{\chi}) + \boldsymbol{\rho}_3(t,\tilde{\boldsymbol{x}})$$
(29)

with

$$\boldsymbol{\rho}_1(t,\tilde{\boldsymbol{x}}) = (\boldsymbol{0}_{3\times1}; \quad \boldsymbol{\rho}_{12}(t,\tilde{\boldsymbol{x}}); \quad \boldsymbol{0}_{3\times1}; \quad \boldsymbol{0}_{2\times1}), \quad (30)$$
$$\boldsymbol{\rho}_2(t,\boldsymbol{\chi}) = (\boldsymbol{0}_{3\times1}; \quad \boldsymbol{0}_{3\times1}; \quad \tilde{\boldsymbol{d}}(t,\boldsymbol{\chi}); \quad \boldsymbol{0}_{2\times1}) \quad (31)$$
$$\boldsymbol{\rho}_3(t,\boldsymbol{\chi}) = \boldsymbol{K}(t)\boldsymbol{\varepsilon}\boldsymbol{y}(t,\tilde{\boldsymbol{x}}), \quad (32)$$

with $\boldsymbol{\rho}_{12}(t,\tilde{\boldsymbol{x}}) = -2\boldsymbol{S}(\boldsymbol{\omega}_{ie}^e)\tilde{\boldsymbol{v}}_{eb}^e + (\boldsymbol{g}_b^e(\boldsymbol{p}_{eb}^e) - \boldsymbol{g}_b^e(\hat{\boldsymbol{p}}_{eb}^e))$ and where,

$$\tilde{\boldsymbol{d}}(t,\boldsymbol{\chi}) = (\boldsymbol{I}_3 - \boldsymbol{R}(\tilde{\boldsymbol{q}})^\mathsf{T})\boldsymbol{R}_b^e\left(\boldsymbol{S}(\boldsymbol{\omega}_{ib}^b)\boldsymbol{f}_{ib}^b + \dot{\boldsymbol{f}}_{ib}^b\right)$$
$$- \boldsymbol{S}(\boldsymbol{\omega}_{it}^e)(\boldsymbol{I}_3 - \boldsymbol{R}^\mathsf{T}(\tilde{\boldsymbol{q}}))\boldsymbol{R}_b^e\boldsymbol{f}_{ib}^b - \boldsymbol{R}^\mathsf{T}(\tilde{\boldsymbol{q}})\boldsymbol{R}_b^e\boldsymbol{S}(\tilde{\boldsymbol{b}}_{\text{ars}}^b)\boldsymbol{f}_{ib}^b.$$
(33)

Moreover, $\boldsymbol{\rho}_3(t,\boldsymbol{\chi})$ stems from linearization errors, similar to [15]. Hence, exponential stability properties, similar to the cited works can be achieved.

Figure 4. Multirotor UAV with GNSS RTK and UWB systems on board.

Additional vertical range measurement—Another option for mitigating the problem with close to linearly dependent line-of-sight vectors, is found in [18], where this issue is handled with the eXogenous Kalman Filter (XKF) [19], linearizing the about an exogenous trajectory from an nonlinear observer. The benefit with this is that the trajectory from the nonlinear observer is globally stable. Thus, the risk of choosing the wrong linearization point in the filter is avoided compared to the EKF where the linearizing is about its own states.

4. EXPERIMENTAL TEST SETUP

The experiments were conducted in a sports field in Trond-heim, Norway, and were carried out using a multirotor equipped with a BeSpoon UM100 [7] UWB impulse radio, a Ublox M8T [20] GNSS receiver, an ADIS16490BMLZ [21] MEMS IMU, shown in Figure 4. The IMU and the GNSS receiver are connected to SenTiBoard (previously SyncBoard) [22], which is a configurable hardware based sensor timing board that uses interrupt capture (IC) to accurately record the time of validity of sensor messages. The BeSpoon UM100 radio is connected to the BeagleBone Black (BBB) Single Board PC (SBPC) running a Linux operating system and LSTS Toolchain software [23]. In the UAV, the BBB is used as the main control device of the whole system including high-level flight control tasks and integration of on-board sensors. A commercial Pixhawk flight controller, running the Ardupilot autopilot software, is used for the low-level control. This also has a built-in magnetometer and an IMU, which it uses in its internal PVA-estimation.

In the area of operation, 5 UWB RTLS anchors and a RTK base station are equipped with the same UWB and GNSS user equipment as in the UAV, seen in Figures 5 and 6. The NED position of the 5 anchors, relative to the RTK base station, can be seen in Table 1. In the anchor devices, the role of the BBB is to send commands and receive data stream from the UWB radio during initialization and inter-anchor measurements. The second task of the anchor's SBPC is management of the RTK GNSS receiver.

The UWB beacons have previously been calibrated by finding their associated antenna offset. This offset is found during the

Figure 5. UWB anchor used during flight tests.

Figure 6. Typical UWB anchors constellation setup during flight tests

initialization of the system by sending this value from Linux user space software to Linux kernel kernel module driver and then via SPI to BeSpoon UM100 UWB chip. The antenna offset value was chosen for anchors and UAV separately for each device. This offset depends on type of used antenna, length of antenna PCB path, length of antenna cable, amount and type of connectors used. After calculation of the antenna offsets, ranging results were empirically tested between devices on different ranges with reference measurements made using measuring tape and laser range finder.

An operation in the UWB network with the UAV, contains two phases: In the initialization phase, the UAV is commanding anchors to perform inter-anchor UWB distance measurements, to determine the relative position of the anchors. The second phase is normal operation, where the UAV is requesting UAV-to-anchors UWB distance measurements. These measurements are based on Time-of-Arrival (TOA) between the UAV and anchors. The ranging accuracy for the UWB system alone is approximately at 10 cm at 800 meters distance between UAV and anchors, at a rate up to 17 Hz. The communication principle for positioning is illustrated in Figure 7. For a complete overview of the setup of the UWB system, see [10]. Communication between UWB radio and BBB is done using SPI, managed by Linux kernel module driver ported on BBB.

It is possible to perform real time estimation of UAV and anchors position, but in the case of these experiment all of the calculations are obtained by post-processing. The measurements on the BBB are synchronized in the DUNE unified navigation environment software [23].

Table 1. UWB anchors NED position.

Anchor	North [m]	East [m]	Down [m]
0	-19.7	-6.6	-0.7
1	87.0	-143.4	0.1
2	100.3	-80.8	-0.8
3	49.1	14.3	-1.3
4	-2.2	-104.6	-2.1

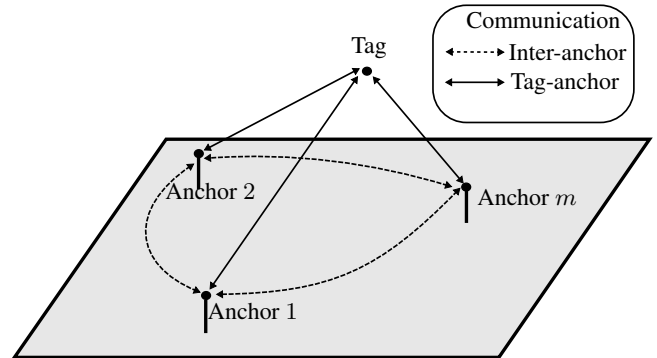It should be noted that the UAV was carried in the experiment.

Figure 7. UWB RTLS communication principle.

5. RESULTS

In the results presented in this section, *TMO* corresponds to the presented observer that only utilize UWB RTLS measurements in the aiding of the IMU, whereas *TMO w/v. range* corresponds to the alternative that also utilize the vertical range measurement.

A comparison of the estimated position and the standalone GPS and RTK-GPS references are plotted in Figure 8 in latitude and longitude, along with the position of the UWB anchors. The temporal evolution of the same data, but transformed to the NED-frame, is shown in Figure 9. Further, Figure 10 shows the position estimate error in the NED-frame, which illustrates the considerable improvement in the case with the vertical range measurement. The innovations corresponding to the different range measurements, including the vertical range, are plotted in Figure 11. All the innovations, except for *anchor 1* which has very few measurements, resemble the bell shape of the normal distribution, indicating that the innovations are Gaussian.

As shown in Figure 14, the UWB clock error estimate is bounded, which indicate that clock does not drift. But the fact that it does not converge to a stationary value, could indicate that it has a colored noise component, or that there are other systematic errors that are being compensated for by this estimate.
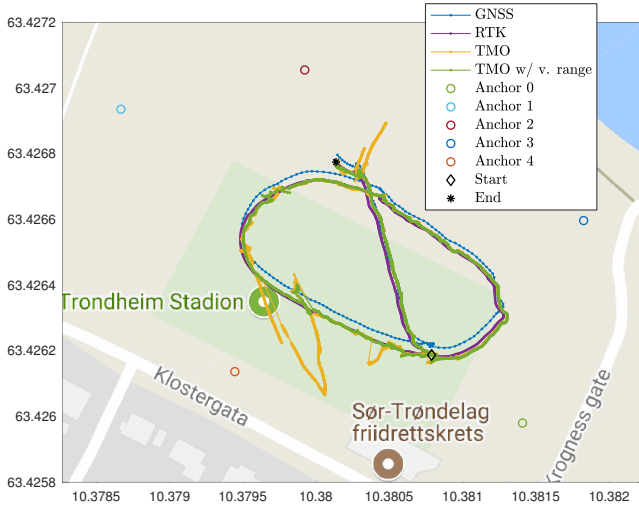
Figure 8. UWB-INS latitude/longitude position estimate, compared to RTK and GNSS. Longitude in degrees is given along the x-axis. Latitude in degrees is given along the y-axis.
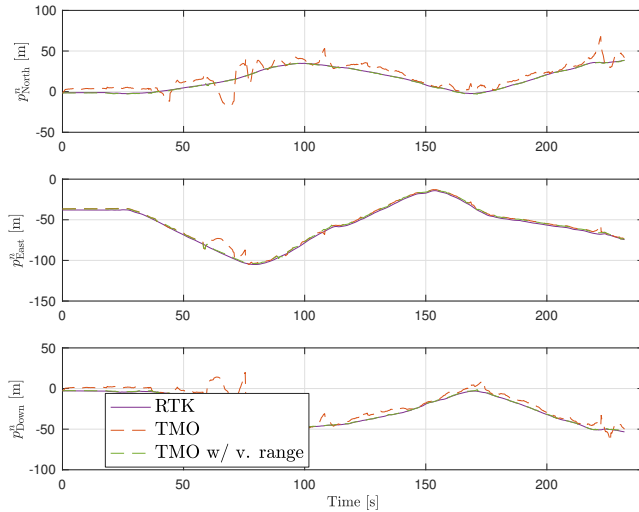

Figure 9. UWB-INS NED position estimate, compared to RTK.

Figure 10. UWB-INS NED position estimate error.

Figure 11. UWB range innovations.

Statistics related to the position estimation relative to RTK can be found in Table 2. The error metrics used are absolute mean error (AME), standard deviation (STD) and root-mean-square (RMS) error. For the case with the additional range measurement, it is apparent that the major component of the position error is in the east direction. This, along with its small standard deviation, indicates that there is a bias that has not been accounted for. This could stem from e.g. inaccuracies in the mounting, as all the anchors where mounted with the same heading.

In evaluating the performance of the attitude observer, it should be pointed out that the reference here is the estimated attitude from the low-cost Pixhawk autopilot. A comparison of the estimated attitude from the presented observer and the Pixhawk reference, as illustrated in Figure 13, shows a generally good resemblance, apart from a short period at around 120 seconds. It should be pointed out that the spikes seen in the yaw error plot are not spikes in the estimate, but come from a slight delay and the wrap between $\pm 180°$. In
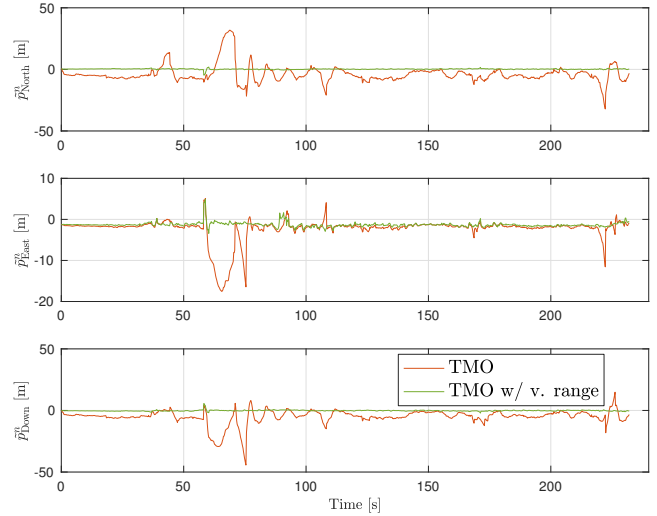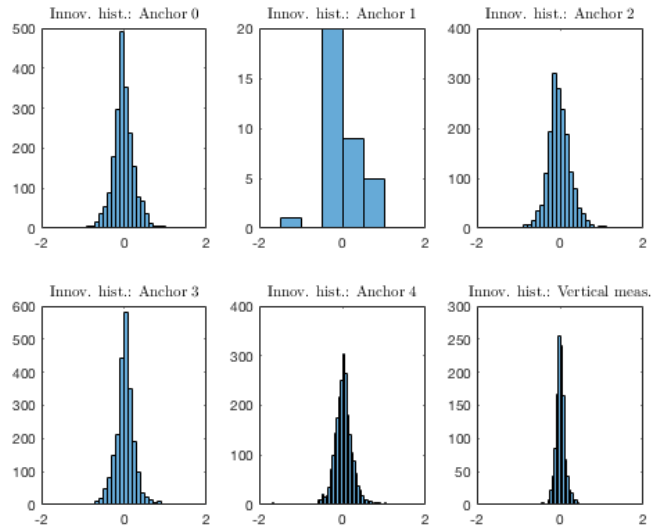
addition to presenting the error in the attitude, relative Pixhawk, Figure 13 compares the attitude errors of the presented observer with and without the vertical range aiding. This shows a slight improvement in the attitude when the vertical range is included. The corresponding attitude error statistics relative the Pixhawk attitude estimate is presented in Table 3.

Due to the lack of ground truth, it is difficult to conclude as to which attitude estimates are the most accurate. In addition, even small errors in the time synchronization might affect the comparison to the Pixhawk reference, due to the fast dynamics of the carried UAV.

At an early stage of the data processing, it was discovered that the innovation terms, $\tilde{y}_{k,\mathrm{UWB}}$, were coloured and heavily biased. Similar to [8], which also use a BeSpoon UWB system, the source of this was found to be repetition of UWB measurements. These repeated measurements have been removed in the preprocessing of the data, while finding the cause of the repetition is a subject for future investigation.

A weakness with the current setup is the timing of the

Table 2. UWB/INS position estimation error relative to RTK in NED coordinates, in meters.

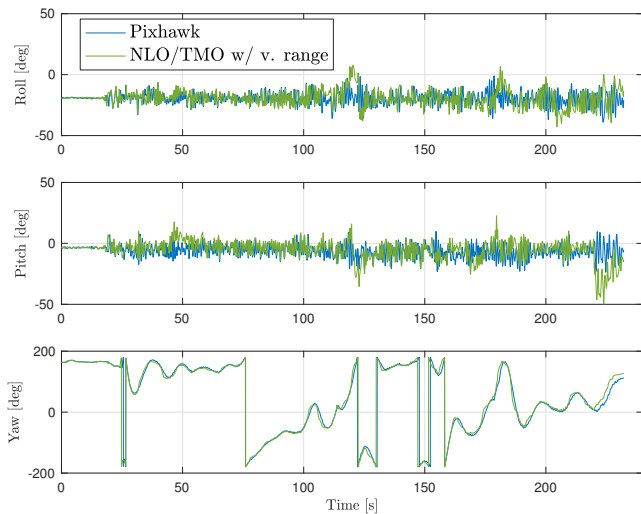| TMO	N [m]	E [m]	D [m]	Norm [m]
AME	6.19	2.42	5.39	8.94
STD	7.05	2.86	5.76	7.57
RMS	8.06	3.70	7.65	11.71
TMO w/v. range				
AME	0.31	1.35	0.32	1.46
STD	0.37	0.55	0.44	0.51
RMS	0.44	1.41	0.47	1.55

Figure 12. UWB-INS Euler angle estimate for the *NLO/TMO w/ v. range*-case, compared to Pixhawk.

Figure 13. UWB-INS Euler angle error estimate, compared to Pixhawk.

Figure 14. UWB clock error estimate.

UWB measurements, which is illustrated in Figure 15, where $M_{m_{UWB}}$ is the time of the UWB measurement, $U_{m_{UWB}}$ is the time of data transmission of said measurement, and $D_{m_{UWB}}$ is the time when the DUNE system is processing the measurement, and associating it with the internal time-stamp. The frequency spectrum is shared between the UWB nodes by using Time Division Multiple Access (TDMA) transmission. The UWB tag in the UAV is currently set up to wait for all m_{UWB} UWB measurements before the measurement packet is sent to the BBB. Additional minor delays $D_{n_{\text{UWB}}} - U_{n_{\text{UWB}}}$ are introduced by the transmission of the UWB measurements from the tag to the SBPC. The temporal grouping of the UWB measurements makes is easier to estimate a position purely based on the UWB measurements, but leads to unnecessary delays $\{\Delta t_{1_{\text{UWB}}} \ldots \Delta t_{m_{\text{UWB}}}\}$ in our setup where the corrector step of the observer is structurally indifferent to the number of measurements in the given time step.

6. SUMMARY

Through data from an outdoor experiment, this paper has demonstrated the accuracy of inertial navigation, aided by an ultra-wideband real time localization system. The ultra wideband pseudorange measurements are fused with acceleration, angular rate and magnetic field measurements, using a tightly coupled integration strategy, in a nonlinear observer. The nonlinear observer is an interconnection of a translational motion observer and an attitude observer, and has exponential stability properties.
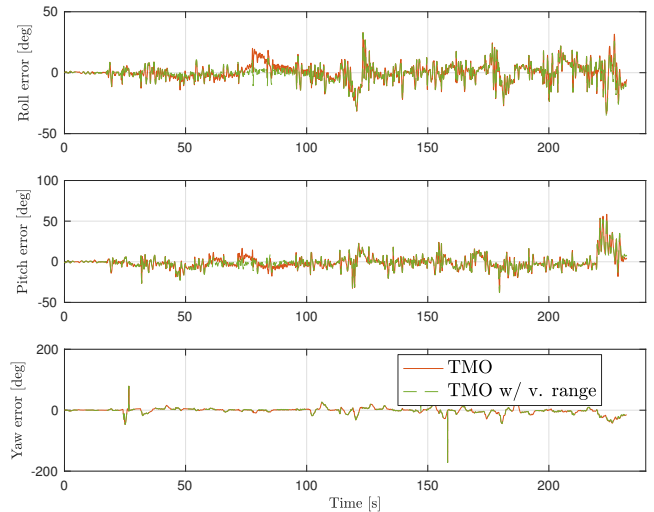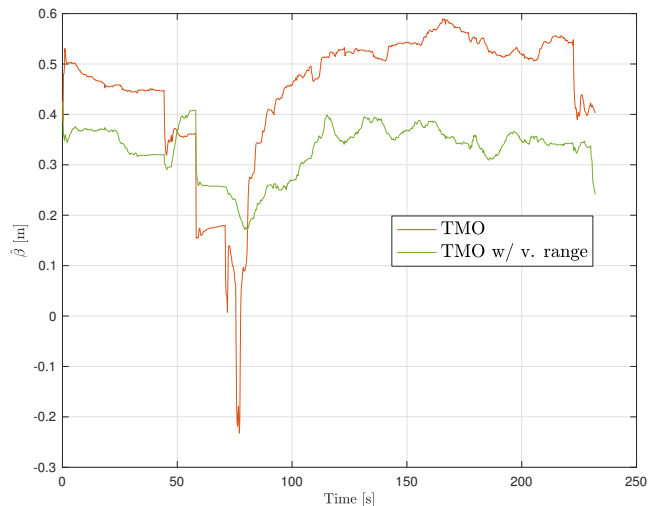
These results show that the UWB-inertial navigation system is a viable solution for local outdoor navigation of UAVs. A substantial reduction of the position error was achieved by including a vertical range measurement, in addition to the UWB ranges. This improved the geometry of the estimation problem, and reduced the average of the position error norm by a factor of 6, to 1.46 meters. The standard deviation and root mean square error values where also significantly reduced. The position error could have been further reduced by compensating for the bias in the east direction. Replacing the linearization about the TMO state, with linearization about the state of a globally stable nonlinear observer, in a similar manner as with the XKF, could possibly also improve the performance of the observer.

Lastly, some weaknesses with the current setup of hardware, that are limiting the performance of the navigation system, have been discussed. These will be the topic for future experiments.

Table 3. UWB/INS attitude error relative to the Pixhawk.

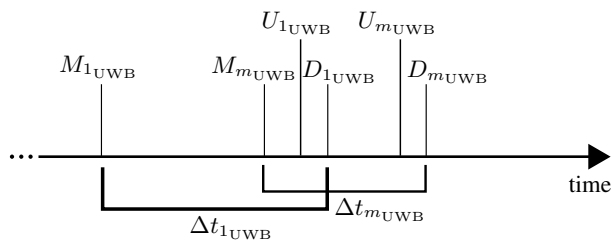| NLO/TMO	**Roll** [deg]	**Pitch** [deg]	**Yaw** [deg]	**Norm** [deg]
AME	5.12	5.55	6.14	11.30
STD	7.31	8.40	10.06	10.08
RMS	7.31	8.44	10.23	15.14
NLO/TMO w/v.range				
AME	4.62	5.30	6.10	10.76
STD	6.88	8.18	10.15	10.25
RMS	6.90	8.22	10.29	14.87

Figure 15. Illustration of the UWB timing issue.

REFERENCES

[1] Y. Feng and J. Wang, "GPS RTK performance characteristics and analysis," *Positioning*, vol. 1, no. 13, p. 0, 2008.

[2] J. M. Wilson, "Ultra-wideband/a disruptive rf technology?" *Version 1.3, Intel Research and Development*, 2002.

[3] H. Cho, T. Kim, Y. Park, and Y. Baek, "Enhanced trajectory estimation method for rtls in port logistics environment," in *2012 IEEE 14th International Conference on High Performance Computing and Communication 2012 IEEE 9th International Conference on Embedded Software and Systems*, June 2012, pp. 1555–1562.

[4] X. Ma and T. Liu, "The application of wi-fi rtls in automatic warehouse management system," in *2011 IEEE International Conference on Automation and Logistics (ICAL)*, Aug 2011, pp. 64–69.

[5] R. Maalek and F. Sadeghpour, "Accuracy assessment of ultra-wide band technology in tracking static resources in indoor construction scenarios," *Automation in Construction*, vol. 30, pp. 170 – 183, 2013.

[6] I. O. for Standardization, "Information technology real-time locating systems (RTLS)," *ISO/IEC 24730-1:2014*, 2014.

[7] BeSpoon, "Full specification of ir-uwb module um100," *Full specification 2.13 AUGUST 2016*, 2016.

[8] H. E. Nyqvist, M. A. Skoglund, G. Hendeby, and F. Gustafsson, "Pose estimation using monocular vision and inertial sensors aided with ultra wide band," in *Indoor Positioning and Indoor Navigation (IPIN), 2015 International Conference on*. IEEE, 2015, pp. 1–10.

[9] A. Conti, M. Guerra, D. Dardari, N. Decarli, and M. Z. Win, "Network experimentation for cooperative localization," *IEEE Journal on Selected Areas in Communications*, vol. 30, no. 2, pp. 467–475, February 2012.

[10] K. P. Cisek, A. P. Zolich, K. Klausen, and T. A. Johansen, "Ultra-wide band real time location systems: Practical implementation and performance evaluation," in *2017 Workshop on Research, Education and Development of Unmanned Aerial Systems (RED-UAS)*, 2017.

[11] K. Gryte, J. M. Hansen, T. A. Johansen, and T. I. Fossen, "Robust navigation of UAV using inertial sensors aided by UWB and RTK GPS," in *AIAA Guidance, Navigation, and Control Conference*, 2017, p. 1035.

[12] E. Fresk, K. Ödmark, and G. Nikolakopoulos, "Ultra wideband enabled inerial odometry for generic localization," in *20th IFAC World Congress*. IFAC, 2017.

[13] M. W. Mueller, M. Hamer, and R. D'Andrea, "Fusing ultra-wideband range measurements with accelerometers and rate gyroscopes for quadrocopter state estimation," in *Robotics and Automation (ICRA), 2015 IEEE International Conference on*. IEEE, 2015, pp. 1730–1736.

[14] H. F. Grip, T. I. Fossen, T. A. Johansen, and A. Saberi, "Nonlinear observer for GNSS-aided inertial navigation with quaternion-based attitude estimation," in *Proc. of the American Contr. Conf.*, Washington, DC, June 2013, pp. 272–279.

[15] T. A. Johansen, J. M. Hansen, and T. I. Fossen, "Nonlinear observer for tightly integrated inertial navigation aided by pseudo-range measurements," *ASME Journal of Dynamic Systems, Measurement and Control*, vol. 139, no. 1, pp. 011 007–011 007–10, 2017.

[16] H. F. Grip, T. I. Fossen, T. A. Johansen, and A. Saberi, "Attitude estimation using biased gyro and vector measurements with time-varying reference vectors," *IEEE Transactions on Automatic Control*, vol. 57, no. 5, pp. 1332—1338, 2012.

[17] M.-D. Hua, G. Ducard, T. Hamel, R. Mahony, and K. Rudin, "Implementation of a nonlinear attitude estimator for aerial robotic vehicles," *IEEE Transactions On Control System Technology*, vol. 22, no. 1, pp. 201–212, 2014.

[18] T. A. Johansen, T. I. Fossen, and G. C. Goodwin, "Three-stage filter for position estimation using pseudo-range measurements," *IEEE Transactions on Aerospace and Electronic Systems*, 2016.

[19] T. A. Johansen and T. I. Fossen, "The eXogenous

kalman filter (xkf)," *International Journal of Control*, 2016.

[20] NEO/LEA-M8T series u-blox M8 concurrent GNSS timing modules. [Online]. Available: https://www.u-blox.com/en/product/neolea-m8t-series

[21] ADIS16490BMLZ - tactical grade, ten degrees of freedom inertial sensor. [Online]. Available: http://www.analog.com/en/products/mems/inertial-measurement-units/adis16490.html

[22] S. M. Albrektsen and T. A. Johansen, "Syncboard - a high accuracy sensor timing board for uav payloads," in *2017 International Conference on Unmanned Aircraft Systems (ICUAS)*, June 2017, pp. 1706–1715.

[23] LSTS toolchain. [Online]. Available: http://lsts.fe.up.pt/toolchain

BIOGRAPHY

Krzysztof Cisek received his M.Sc. (Eng.) degrees in control engineering and robotics from the Wrocaw University of Science and Technology, Faculty of Electronics, in 2011. From 2011 to 2014 he was software and robotics engineer in R&D Department in Flytronic Sp. z o.o. (WB Group), leading Polish constructor and R&D center for Unmanned Aerial Vehicles and Systems for defense sector, Gliwice, Poland. From 2014 he is research fellow and engineer at Unmanned Aerial Vehicle Laboratory, Autonomous Marine Operations and Systems (AMOS), Department of Cybernetics at Norwegian University of Science and Technology. His research interests are in the areas of software/hardware development and integration of unmanned aerial systems, ultra wideband location systems and data fusion. This work is supervised by professor Tor Arne Johansen.

Kristoffer Gryte received his received his M.Sc. in Engineering Cybernetics in 2015 at the Norwegian University of Science and Technology, within guidance, navigation and control of vehicles. He is currently pursuing a PhD related to UAV technology, focusing on autonomous landing of fixed-wing UAVs. This work is supervised by professor Thor Inge Fossen and professor Tor Arne Johansen.

Torleiv H. Bryne received the M.Sc. and Ph. D. degree in Engineering Cybernetics from the Norwegian University of Science and Technology, Department of Engineering Cybernetics, in 2013 and 2017. He is currently employed as post-doctoral researcher at the same department. His research interests are in the areas of estimation, in particular applied in the context of navigation. UAVs and marine applications are the main focus areas of his research.

Tor A. Johansen (M'98-SM'01) received the M.Sc. and Ph.D. degrees in electrical and computer engineering from the Norwegian University of Science and Technology (NTNU), Trondheim, Norway, in 1989 and 1994, respectively. From 1995 to 1997, he was with SINTEF, Trondheim, Norway, as a Researcher. He was an Associate Professor at NTNU in 1997 and a Professor in 2001. In 2002, he co-founded the company Marine Cybernetics AS, where he was a Vice President until 2008. He is currently a Principal Researcher with the Center of Excellence on Autonomous Marine Operations and Systems, and the Director of the Unmanned Aerial Vehicle Laboratory at NTNU. He has authored several articles in the areas of control, estimation, and optimization with applications in the marine, automotive, biomedical and process industries. Prof. Johansen was a recipient of the 2006 Arch T. Colwell Merit Award of the SAE.